

# Multiparametric Cardiac $^{18}\text{F}$ -FDG PET in Humans: Pilot Comparison of FDG Delivery Rate with $^{82}\text{Rb}$ Myocardial Blood Flow

Yang Zuo<sup>1</sup>, Javier E. López<sup>2</sup>, Thomas W. Smith<sup>2</sup>, Cameron C. Foster<sup>1</sup>, Richard E. Carson<sup>3</sup>, Ramsey D. Badawi<sup>1,4</sup>, Guobao Wang<sup>1</sup>

1. Department of Radiology, University of California Davis Medical Center, CA 95817, United States

2. Department of Internal Medicine, University of California Davis Medical Center, CA 95817, United States

3. Department of Radiology and Biomedical Imaging, Yale University, New Haven, CT 06520, United States

4. Department of Biomedical Engineering, University of California at Davis, United States

E-mail: gbwang@ucdavis.edu

**Abstract.** Myocardial blood flow (MBF) and flow reserve are usually quantified in the clinic with positron emission tomography (PET) using a perfusion-specific radiotracer (e.g.  $^{82}\text{Rb}$ -chloride). However, the clinical accessibility of existing perfusion tracers remains limited. Meanwhile,  $^{18}\text{F}$ -fluorodeoxyglucose (FDG) is a commonly used radiotracer for PET metabolic imaging without similar limitations. In this paper, we explore the potential of  $^{18}\text{F}$ -FDG for myocardial perfusion imaging by comparing the myocardial FDG delivery rate  $K_1$  with MBF as determined by dynamic  $^{82}\text{Rb}$  PET in fourteen human subjects with heart disease. Two sets of FDG  $K_1$  were derived from one-hour dynamic FDG scans. One was the original FDG  $K_1$  estimates and the other was the corresponding  $K_1$  values that were linearly normalized for blood glucose levels. A generalized Renkin-Crone model was used to fit FDG  $K_1$  with Rb MBF, which then allowed for a nonlinear extraction fraction correction for converting FDG  $K_1$  to MBF. The linear correlation between FDG-derived MBF and Rb MBF was moderate ( $r=0.74$ ) before the glucose normalization and became much improved ( $r=0.92$ ) after glucose normalization. The extraction fraction of FDG was also similar to that of Rb-chloride in the myocardium. The results from this pilot study suggest that dynamic cardiac FDG-PET with tracer kinetic modeling has the potential to provide MBF in addition to its conventional use for metabolic imaging.

## 1. Introduction

Myocardial perfusion (blood flow) imaging with positron emission tomography (PET) has been applied in clinical cardiology to diagnose and characterize cardiovascular diseases [1–4]. Various perfusion radiotracers (e.g.,  $^{15}\text{O}$ -water,  $^{13}\text{N}$ -ammonia,  $^{82}\text{Rb}$ -chloride,  $^{11}\text{C}$ -acetate) have been used [5]. Despite their potentials, the accessibility to these flow tracers remains limited for clinical use. For example,  $^{15}\text{O}$ -water is the gold standard for measuring blood

flow [6, 7] but its half-life is very short (2.05 minutes), requiring onsite cyclotron for tracer production and is not approved for routine clinical use.  $^{13}\text{N}$ -ammonia [8,9] and  $^{82}\text{Rb}$ -chloride [10, 11, 13, 14] are the two blood flow radiotracers routinely used in clinical practice [5]. However,  $^{13}\text{N}$ -ammonia also requires an onsite or nearby cyclotron due to its short half-life of 10 minutes.  $^{82}\text{Rb}$ -chloride can be produced by a mobile generator despite its short half-life (76 seconds). Nevertheless, the cost of a rubidium generator is  $\geq$  \$30,000 for every 4-6 weeks; this is only affordable to those hospitals or centers with a high throughput of cardiac patients [3,15].  $^{11}\text{C}$ -acetate is another promising tracer [16–18] but its 20-minute half-life still requires a nearby cyclotron. Together, these practical challenges limit the access to perfusion imaging by PET.

$^{18}\text{F}$ -fluorodeoxyglucose (FDG), which has a longer half-life of 110 minutes, is the most broadly used clinical PET radiotracer, mainly for metabolic imaging [15]. In clinical cardiology,  $^{18}\text{F}$ -FDG PET is commonly used in combination with a short half-life flow tracer to evaluate flow-metabolism mismatch in the myocardium [19]. Such a two-tracer PET method is the gold standard for assessing myocardial viability [20] and inflammatory conditions such as cardiac sarcoidosis [21]. The method is not widely available in the clinic because of the limited accessibility of current flow-specific radiotracers. While the new flow tracer  $^{18}\text{F}$ -fluopiridaz [22] does not have the accessibility problem, it may result in longer clinic visit times when combined with  $^{18}\text{F}$ -FDG for myocardial flow-metabolism imaging because of the long half-life of the  $^{18}\text{F}$  isotope in the two different tracers.

The hypothesis of this study is that dynamic cardiac  $^{18}\text{F}$ -FDG PET imaging as a single tracer imaging can provide myocardial blood flow in addition to myocardial glucose metabolism by use of tracer kinetic modeling. The successful testing of this hypothesis may allow simultaneous imaging of myocardial blood flow and glucose metabolism only using  $^{18}\text{F}$ -FDG without the need for a second flow-specific tracer. Once validated, this single-tracer (i.e., FDG) multiparametric (i.e., flow and metabolism) imaging method has the potential to enable evaluation of myocardial viability and myocardial inflammation with reduced imaging time, cost and radiation exposure as compared to the traditional two-tracer methods in clinical practice today [3, 15].

The potential of  $^{18}\text{F}$ -FDG for blood flow imaging has been explored outside cardiac imaging. By use of tracer kinetic modeling [23], several studies have shown that the FDG blood-to-tissue delivery rate  $K_1$  correlates with blood flow in tumors [24–28]. For example, Tseng *et al.* [24] demonstrated linear correlations between  $K_1$  of 60-minute dynamic FDG-PET and  $^{15}\text{O}$ -water blood flow in breast tumors, with a linear correlation coefficient  $r=0.62$  before neoadjuvant chemotherapy and  $r=0.81$  after the therapy. Later, Mullani *et al.* [25] reported that for various types of tumor in 16 patients, regional tumor FDG  $K_1$  estimated from a 2-minute first-pass dynamic PET scan has a correlation  $r=0.86$  with the blood flow measured by  $^{15}\text{O}$ -water PET. Correlation of FDG  $K_1$  to blood flow has also been reported in organs such as liver and brain [29, 30]. In pigs, hepatic FDG  $K_1$  derived from a 3-minute early-dynamic FDG-PET scan correlated with hepatic blood flow measured by transit time flow meters with a high correlation  $r=0.94$  [29]. In a rat model of stroke, Walberer *et al.* also reported that cerebral FDG  $K_1$  estimated by one-hour dynamic PET data had a correlation

of  $r=0.86$  with  $^{15}\text{O}$ -water blood flow [30]. These studies support the potential use of  $^{18}\text{F}$ -FDG for estimating blood flow, though the effectiveness of  $^{18}\text{F}$ -FDG  $K_1$  likely depends on the specific tissue types; this is because FDG extraction fraction varies in different tissue and is also dependent on blood flow.

Our work is specifically focused on *myocardial* blood flow imaging using  $^{18}\text{F}$ -FDG. There is no prior study yet attempting to demonstrate the effectiveness of FDG flow in the myocardium. The importance of this work relies in the possible application of myocardial FDG flow to myocardial flow-metabolism mismatch evaluation for myocardial viability and inflammation and potentially more broadly, to rest-stress perfusion imaging for diagnosis ischemic heart disease. Toward that end, our previous work specifically evaluated the practical identifiability of myocardial FDG  $K_1$  quantification under different scan durations [31]. The results showed it is feasible to quantify FDG  $K_1$  in the myocardium using appropriate kinetic modeling.

The purpose of this paper is to directly compare myocardial FDG  $K_1$  with MBF that is determined by a flow-specific tracer in human patients with heart disease. One challenge for using FDG to assess myocardial blood flow is the association of this glucose analog with blood glucose levels. As demonstrated in this paper, this may in turn compromise the performance of FDG  $K_1$  for deriving MBF. To address this challenge, we also propose a glucose normalization approach to adjusting FDG  $K_1$  that can reduce the effect of blood glucose levels.

## 2. Methods

### 2.1. Dynamic $^{18}\text{F}$ -FDG PET and Dynamic $^{82}\text{Rb}$ PET Data Acquisition

Fourteen patients with ischemic heart disease (IHD) or suspected cardiac sarcoidosis were referred for PET myocardial viability or inflammation assessment by PET and enrolled into this study after giving informed consent. The study is approved by Institutional Review Board at the University of California, Davis. Each patient underwent a dynamic  $^{82}\text{Rb}$ -PET/CT scan first and then a dynamic FDG-PET/CT scan, both scans operated on a GE Discovery ST PET/CT scanner in two-dimensional mode. The time between the Rb scan and FDG scan ranges from a few minutes to one hour, depending on the oral glucose loading procedure.

For dynamic Rb-PET imaging, patients received approximately 30 mCi  $^{82}\text{Rb}$ -chloride with a bolus injection. A low-dose transmission CT scan was performed at the beginning of PET scan to provide CT images for PET attenuation correction. The dynamic scan lasted for nine minutes. The acquired raw data were binned into 16 dynamic frames:  $12 \times 10$  s,  $2 \times 30$  s,  $1 \times 60$  s,  $1 \times 300$  s. Dynamic Rb-PET images were reconstructed using the standard ordered-subset expectation-maximization (OSEM) algorithm. All data corrections, including normalization, dead-time correction, attenuation correction, scatter correction, and random correction, were included in the reconstruction process.

For dynamic FDG-PET imaging, patients received approximately 20 mCi  $^{18}\text{F}$ -FDG with a bolus injection. Data acquisition was commenced right after the FDG injection and lasted

for 60 minutes. The acquired raw data were then binned into a total of 49 dynamic frames:  $30 \times 10$  s,  $10 \times 60$  s and  $9 \times 300$  s. Other processing was the same as the Rb-PET scans.

## 2.2. Kinetic Modeling of Cardiac $^{18}\text{F}$ -FDG PET Data

An ellipsoidal region of interest (ROI) was manually placed in the left ventricle (LV) to extract a blood time activity curve  $C_{LV}(t)$ . An additional 17 ROIs were placed within the 17 segments of myocardium according to the AHA-17 standard [32]. These segment ROIs were combined into a global myocardial ROI and used to extract a global myocardial TAC  $C_T(t)$  using ROI mean. Due to high noise of the dynamic data in individual segments, the analysis of this study was focused on global myocardial quantification. Based on the analysis in our previous work [31], a reversible two-tissue compartmental model [23] was used to model the one-hour dynamic FDG-PET data:

$$\frac{dC_1(t)}{dt} = K_1 C_p(t) - (k_2 + k_3)C_1(t) + k_4 C_2(t), \quad (1)$$

$$\frac{dC_2(t)}{dt} = k_3 C_1(t) - k_4 C_2(t), \quad (2)$$

where  $C_p(t)$  is the FDG concentration in the plasma,  $C_1(t)$  is the concentration of free FDG and  $C_2(t)$  denotes the activity concentration of metabolized tracer in the myocardium tissue space.  $K_1$  is the tracer delivery rate from the blood space to the tissue space with the unit mL/min/mL;  $k_2$  (/min) is the rate constant of tracer exiting the tissue space;  $k_3$  (/min) is phosphorylation rate;  $k_4$  (/min) is the dephosphorylation rate. With  $v_b$  denoting the fractional blood volume and  $C_{wb}(t)$  denoting the activity in the whole blood, the total activity that is measured by PET is described by

$$C_T(t) = (1 - v_b)[C_1(t) + C_2(t)] + v_b C_{wb}(t). \quad (3)$$

In this work, both  $C_p(t)$  and  $C_{wb}(t)$  were set to  $C_{LV}(t)$ . The unknown kinetic parameters ( $v_b$ ,  $K_1$ ,  $k_2$ ,  $k_3$ ,  $k_4$ ) were estimated using nonlinear least-square curve fitting. Their initial values were set to (0.1,0.1,0.1,0.1,0.001). The lower bounds were zeros and the upper bounds were (1.0,2.0,2.0,1.0,0.1) based on our previous practical identifiability analysis in [31].

## 2.3. Adjustment of FDG $K_1$ with Glucose Normalization

Our theoretical analysis in the Appendix indicates that FDG  $K_1$  can relate to the blood glucose level  $C_{\text{glu}}$  by

$$K_1 \triangleq f(C_{\text{glu}}) \approx f(C_{\text{glu},0}) + \dot{f}(C_{\text{glu},0}) \cdot (C_{\text{glu}} - C_{\text{glu},0}), \quad (4)$$

where  $f(\cdot)$  is a nonlinear function of  $C_{\text{glu}}$  determined from the Renkin-Crone model and Michaelis-Menten model [23], see Eq. (15) in the Appendix.  $C_{\text{glu},0}$  denotes a reference blood glucose level and  $\dot{f}(\cdot)$  is the first-order derivative of  $f$ . Based on the theoretical derivations in the Appendix, we have derived that

$$\dot{f}(C_{\text{glu},0}) < 0. \quad (5)$$

This suggests FDG  $K_1$  is inversely correlated with the blood glucose level,

$$K_1 \approx -s \cdot C_{\text{glu}} + \text{int}, \quad (6)$$

where  $s \triangleq -\dot{f}(C_{\text{glu},0})$  denotes the absolute slope ( $s > 0$ ) and  $\text{int}$  is the intercept of the plot of FDG  $K_1$  with respect to  $C_{\text{glu}}$ . Practically,  $s$  can be estimated using a correlation analysis between the measured FDG  $K_1$  and  $C_{\text{glu}}$  data.

To reduce the dependency of FDG  $K_1$  on  $C_{\text{glu}}$ , we consider  $f(C_{\text{glu},0})$  as an adjusted FDG  $K_1$ . Based on Eq. (4), it can be calculated using the following form

$$K_1^{\text{adj}} \triangleq f(C_{\text{glu},0}) = K_1 + s \cdot (C_{\text{glu}} - C_{\text{glu},0}), \quad (7)$$

in which the blood glucose level of a patient is normalized and used to adjust the value of FDG  $K_1$  linearly. A similar linear correction was used by Stout *et al.* [33] for reducing the effects of normal physiological concentration of plasma large neutral amino acids on the  $K_1$  of 6-[F-18]Fluoro-L-3,4-dihydroxyphenylalanine (FDOPA). As normal blood glucose levels range between 80-120 mg/dL, we use  $C_{\text{glu},0} = 100$  mg/dL in this work.

#### 2.4. Reference MBF by Dynamic Rb-PET

Similar to the analysis of dynamic FDG-PET data described above, ROIs were drawn in the LV cavity and myocardium regions to extract regional TACs from the dynamic Rb-PET images. The myocardial TAC was modeled using a one-tissue compartmental model [11] with the following expression:

$$C_T(t) = (1 - v_b)C_1(t) + v_b C_{wb}(t), \quad (8)$$

where  $C_1(t)$  denotes the concentration of  $^{82}\text{Rb}$  in the tissue compartment with  $K_1$  and  $k_2$  now representing the rate constants of  $^{82}\text{Rb}$  transport between the plasma space and tissue space. This one-tissue model is equivalent to the two-tissue model in Eq. (2) with  $k_3 = 0, k_4 = 0$ . All the  $^{82}\text{Rb}$  kinetic parameters ( $v_b, K_1, k_2$ ) were estimated using nonlinear least-square curve fitting in a way similar to [31].

The estimated Rb  $K_1$  was then converted into myocardial blood flow MBF using the generalized Renkin-Crone model following Lortie's formula for  $^{82}\text{Rb}$ -PET data [11]:

$$K_{1,\text{RB}} = \text{MBF} \cdot \left[ 1 - a_{\text{RB}} \cdot \exp\left(-\frac{b_{\text{RB}}}{\text{MBF}}\right) \right] \quad (9)$$

where  $a_{\text{RB}} = 0.77$  and  $b_{\text{RB}} = 0.63$  (mL/min/mL). MBF is derived from Rb  $K_1$  through a look-up table that is pre-generated using the model.

#### 2.5. Extraction Fraction Correction (EFC) for Converting FDG $K_1$ to MBF

Similar to the conversion Eq. (9) for  $^{82}\text{Rb}$ -chloride, we can apply the generalized Renkin-Crone model to fit the FDG  $K_1$  and MBF data under the assumption that capillary recruitment is involved at higher flow [12],

$$K_{1,\text{FDG}} = \text{MBF} \cdot \left[ 1 - a_{\text{FDG}} \cdot \exp\left(-\frac{b_{\text{FDG}}}{\text{MBF}}\right) \right], \quad (10)$$

where  $a_{\text{FDG}}$  and  $b_{\text{FDG}}$  are to be estimated from the paired data of FDG  $K_1$  and Rb MBF using nonlinear least square fitting. The initial values for the two parameters  $a_{\text{FDG}}$  and  $b_{\text{FDG}}$  were both set to 0.1. Note that if  $a_{\text{FDG}}$  is fixed at 1.0, then the model is equivalent to the classic Renkin-Crone model without capillary recruitment.

The first-pass extraction fraction of FDG is defined by

$$E_{\text{FDG}} \triangleq \frac{K_{1,\text{FDG}}}{\text{MBF}}. \quad (11)$$

Theoretically it relates to MBF following the generalized Renkin-Cone model, i.e.,

$$E_{\text{FDG}} = 1 - a_{\text{FDG}} \cdot \exp\left(-\frac{b_{\text{FDG}}}{\text{MBF}}\right). \quad (12)$$

The effect of flow-dependent FDG extraction fraction can be corrected using the inverse function of Eq. (10), leading to more quantitative FDG-derived MBF from FDG  $K_1$ . Similar to  $^{82}\text{Rb}$ -chloride, the nonlinear conversion from FDG  $K_1$  to MBF is performed through a look-up table using Eq. (10) with predetermined  $a_{\text{FDG}}$  and  $b_{\text{FDG}}$ . The EFC was separately performed for the original FDG  $K_1$  (i.e., without glucose normalization) and the adjusted FDG  $K_1$  (i.e., with glucose normalization).

## 2.6. Statistical Correlation Analysis

We used the Pearson's correlation analysis approach to analyze the potential correlation between FDG  $K_1$  and MBF and biological variables such as age (years), body mass index (BMI) ( $\text{kg}/\text{m}^2$ ), and blood glucose (BG) level ( $\text{mg}/\text{dL}$ ). A p value  $\leq 0.05$  was considered as statistically significant. All the analyses were done using MATLAB (MathWorks, MA).

## 3. Results

### 3.1. Patient Characteristics

Patient characteristics are provided in table 1. Among the fourteen patients enrolled in the study, ten were diagnosed as ischemic heart disease and four were diagnosed with or suspected of cardiac sarcoidosis prior to the scans. All of the patients completed the dynamic  $^{82}\text{Rb}$ -PET scan. Twelve patients had a dynamic FDG-PET scan of 50-60 minutes. Two other patients had a dynamic FDG-PET scan of only 30-40 minutes due to discomfort, and therefore these two subjects were not included in this study.

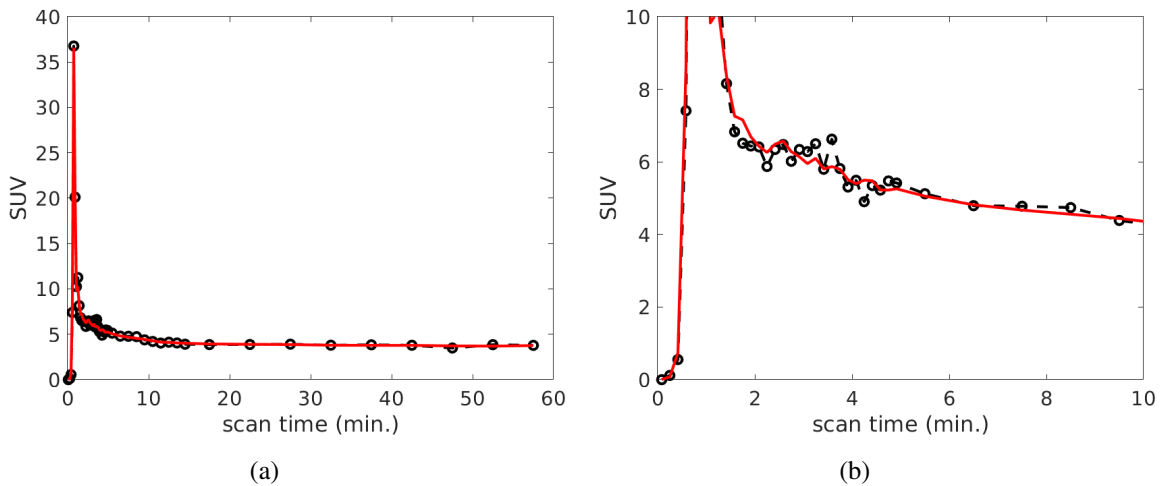
Other characteristics of the patients, including age, sex, diabetic status, BMI, BG level (before PET imaging), and dynamic FDG-PET scan duration are also reported in table 1. Unavailable data is marked with '/' in the table.

### 3.2. Myocardial TAC Fitting and Kinetics

Fig. 1 shows an example of myocardial FDG TAC fitting for the 1-hour data. The fit demonstrated a good match between the measured time points and predicted TAC by the model. The estimated  $^{18}\text{F}$ -FDG kinetic parameters and  $^{82}\text{Rb}$ -chloride MBF values of all the

**Table 1.** Characteristics of the patients enrolled in the study.

Patient	IHD	Age (years)	Sex	Diabetic	BMI	BG (mg/dL)	FDG Scan Time (min)
1	Y	58	M	Y	38.6	127	60
2	Y	73	M	N	24.4	113	50
3	Y	61	M	N	33.9	88	60
4	N	71	F	N	22.4	116	60
5	Y	55	F	N	24.5	118	40
6	N	57	M	N	27.4	/	60
7	Y	63	M	N	28.8	105	60
8	Y	59	M	Y	28.3	135	60
9	Y	65	M	Y	27.2	130	50
10	N	81	M	N	25.8	85	60
11	Y	74	M	N	28.2	84	60
12	Y	83	M	N	33.6	/	60
13	Y	59	M	Y	35.9	107	60
14	N	69	F	N	31.4	82	30

**Figure 1.** Example of myocardial TAC fitting of the 60-minute dynamic FDG data. (a) full plot; (b) zoom-in of the first 10 minutes.

patients are summarized in table 2. For the FDG protocol, the results of two patients were not available due to an incomplete dynamic FDG scan. The average values of the absolute bias and standard deviation (SD) across the twelve patients are reported in table 3 for each of the FDG kinetic parameters. The estimation errors were obtained using the practical identifiability analysis, see [31] for details. The result indicates that FDG  $K_1$  was able to be estimated with a small bias ( $< 3\%$ ) and low SD ( $< 12\%$ ).

### 3.3. Correlation of FDG $K_1$ with Blood Glucose and Other Biological Variables

Table 4 summarizes the Pearson's  $r$  and  $p$  values between FDG  $K_1$  and the biological variables including age, BMI, and BG level. The results of MBF were also included in the table for

**Table 2.** Estimates of FDG kinetics and  $^{82}\text{Rb}$ -chloride MBF

Patient No.	$^{18}\text{F}$ -FDG					$^{82}\text{Rb}$ -chloride		FDG $K_1$ after adjustment for BG
	$v_b$	$K_1$	$k_2$	$k_3$	$k_4$	$v_b$	MBF	
1	0.603	0.138	0.399	0.021	0.027	0.446	0.440	0.293
2	0.249	0.440	1.068	0.129	0.017	0.374	0.651	0.515
3	0.380	0.675	2.000	0.176	0.022	0.389	0.904	0.607
4	0.279	0.681	2.000	0.061	0.027	0.304	1.842	0.773
5	/	/	/	/	/	0.366	0.674	/
6	0.368	0.593	2.000	0.041	0.081	0.411	0.812	0.593
7	0.494	0.279	1.059	0.091	0.054	0.377	0.432	0.308
8	0.371	0.284	0.690	0.107	0.043	0.362	0.642	0.485
9	0.461	0.366	0.795	0.056	0.017	0.336	0.700	0.538
10	0.328	0.667	1.976	0.222	0.031	0.359	0.953	0.581
11	0.260	0.413	1.266	0.072	0.026	0.311	0.617	0.321
12	0.391	0.584	1.539	0.061	0.032	0.294	0.633	0.584
13	0.591	0.302	0.616	0.046	0.026	0.502	0.541	0.342
14	/	/	/	/	/	0.428	1.004	/

**Table 3.** Mean absolute bias and SD of the estimates of FDG kinetics

	$v_b$	$K_1$	$k_2$	$k_3$	$k_4$
Bias (%)	0.3	2.7	3.6	4.9	2.9
SD (%)	2.9	11.4	14.1	23.1	15.1

**Table 4.** Pearson's  $r$  and  $p$  of FDG  $K_1$  and MBF with patients' age, BMI, and blood glucose (BG) concentration.

Biological Variables		Age	BMI	BG
FDG $K_1$	$r$	0.495	-0.443	-0.562
	$p$	0.102	0.150	0.091
$^{82}\text{Rb}$ MBF	$r$	0.237	-0.565	-0.076
	$p$	0.458	0.055	0.835

comparison. The estimated fractional blood volume  $v_b$  of FDG was not exactly equal to the  $v_b$  of Rb as shown in table 2, but the two parameters correlated well with each other with statistical significance ( $r=0.696$ ,  $p=0.012$ ).

FDG  $K_1$  did not correlate with age and BMI. MBF tended to inversely correlate with BMI ( $r=-0.565$ ,  $p=0.055$ ). FDG  $K_1$  tended to inversely correlate with BG ( $r=-0.562$ ,  $p=0.091$ ) as also shown in Fig. 2(a), while a similar trend was not observed for MBF ( $r=-0.076$ ,  $p=0.835$ ). The negative correlation between FDG  $K_1$  and BG demonstrates a proof of the theoretical derivation in Eq. (6).

The estimated slope  $s$  between FDG  $K_1$  and BG was 0.0057, with which the original FDG  $K_1$  was then adjusted for blood glucose levels using Eq. (7) with a reference  $C_{\text{glu},0} = 100$  mg/dL. The FDG  $K_1$  after the adjustment is included in table 2. Note that the adjustment was not applied if a BG value was unavailable. The linear dependency of FDG  $K_1$  on blood



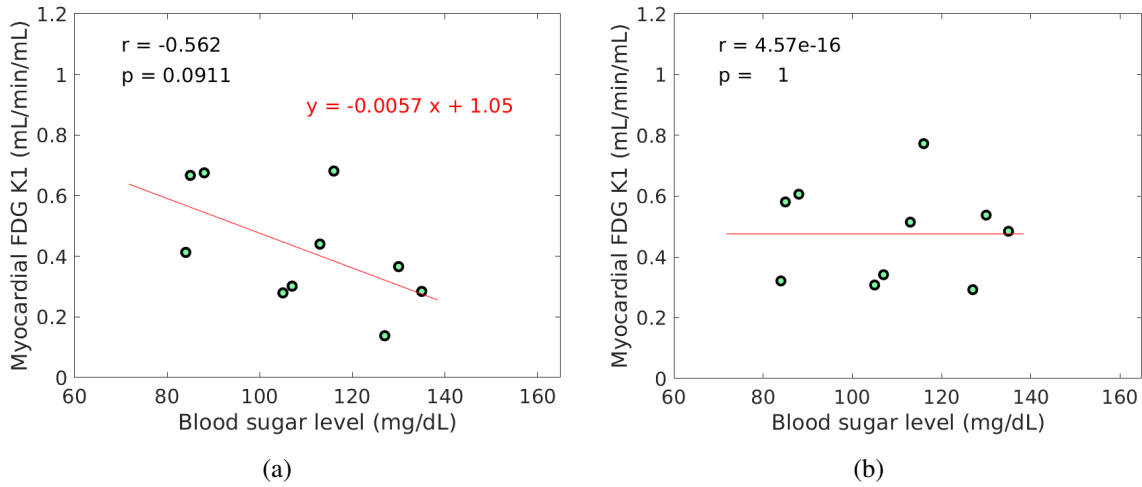


**Figure 2.** Correlation between FDG  $K_1$  and blood glucose level (a) before and (b) after FDG  $K_1$  is adjusted for blood glucose levels.

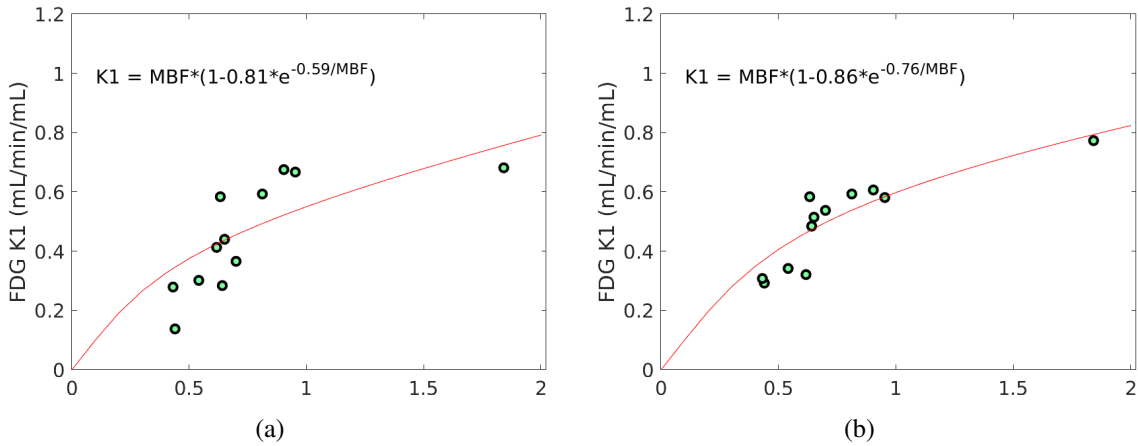


**Figure 3.** Nonlinear association between FDG  $K_1$  and MBF before (a) and after (b) FDG  $K_1$  is adjusted for blood glucose levels.

glucose diminished with the glucose normalization. Fig. 2(b) shows that the linear inverse correlation no longer exists between the adjusted FDG  $K_1$  and blood glucose levels. Both of these two sets of FDG  $K_1$  will be used in the subsequent analysis.

### 3.4. Nonlinear Conversion from FDG $K_1$ to MBF

Fig. 3 shows the nonlinear association of FDG  $K_1$  with MBF before and after the adjustment of FDG  $K_1$  for blood glucose. For both cases, the data were fitted using the generalized Renkin-Crone model Eq. (10). The estimated  $a_{\text{FDG}}$  and  $b_{\text{FDG}}$  values are also shown in the figure.

Using the fitted model for extraction fraction correction, FDG  $K_1$  was converted to MBF in each case based on Eq. (10). Fig. 4 shows the results of linear correlation between FDG-

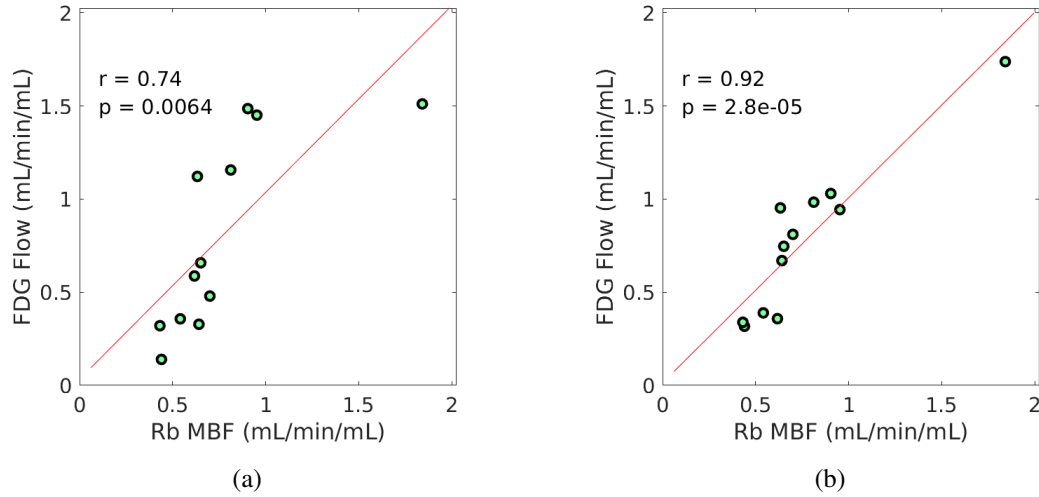


**Figure 4.** Correlation between FDG MBF and Rb MBF before (a) and after (b) FDG  $K_1$  is adjusted for blood glucose levels.

**Table 5.** Mean and standard deviation of Rb MBF and FDG MBF in IHD and non-IHD patients. Unit: mL/min/mL

	IHD	non-IHD
$^{82}\text{Rb}$ MBF	0.618±0.143	1.202±0.558
FDG MBF without $K_1$ adjustment	0.609±0.433	1.373±0.190
FDG MBF with $K_1$ adjustment	0.624±0.280	1.222±0.448

derived MBF and Rb MBF. Both correlations were statistically significant ( $p < 0.01$ ). The correlation coefficient was moderate ( $r = 0.74$ ) without adjusting FDG  $K_1$  for blood glucose, and became much improved ( $r = 0.92$ ) after the adjustment.

Table 5 further compares the statistics (mean and SD) of Rb MBF and FDG-derived MBF in the ischemic heart disease (IHD) group (9 patients) and non-IHD group (3 patients). The mean and SD became closer to that of Rb MBF after the adjustment of FDG  $K_1$  for blood glucose in both groups.

### 3.5. Myocardial Extraction Fraction of FDG

Fig. 5 shows the extraction fraction of FDG in the myocardium as a function of MBF using the FDG  $K_1$  estimates with and without normalization for blood glucose levels. Both the measured  $E_{\text{FDG}}$  using Eq. (11) and the calculated model Eq. (12) are shown. The theoretical extraction fraction of Rb-chloride in the myocardium [11] is also included for comparison. The results show that the relation of the extraction fraction of FDG with respect to MBF was close to that of Rb-chloride in a range of MBF between 0-2 mL/min/mL.

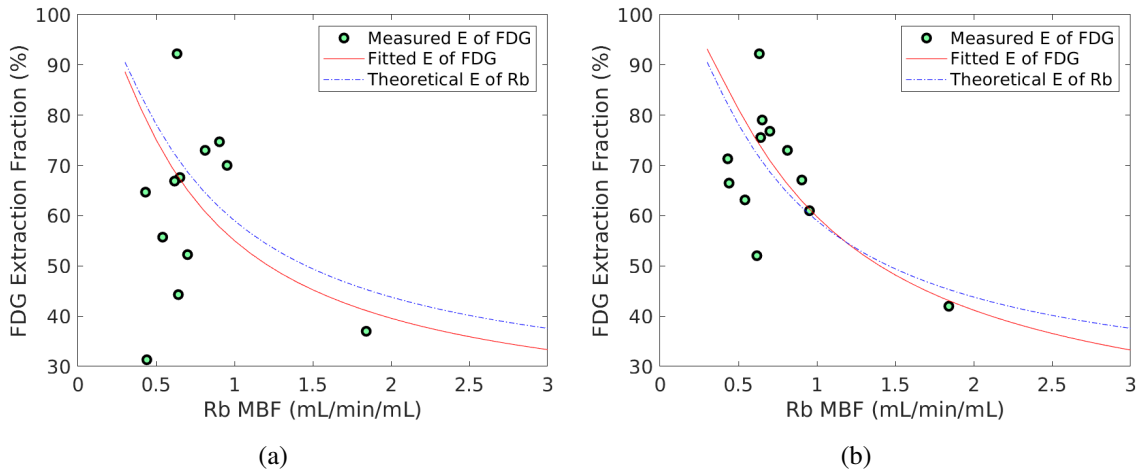


**Figure 5.** Extraction fraction of FDG in the myocardium as compared to Rb MBF without (a) and with (b) adjusting FDG  $K_1$  for blood glucose levels.

#### 4. Discussion

In this paper, we investigated the feasibility of  $^{18}\text{F}$ -FDG for assessing MBF through a pilot clinical study. The FDG delivery rate  $K_1$  demonstrated an inverse linear correlation with blood glucose levels according to both the theoretical investigation in Eq. (6) and patient data shown in Fig. 2(a). We therefore proposed a glucose normalization approach to adjusting FDG  $K_1$  for removing the linear dependence of FDG  $K_1$  on blood glucose (Fig. 2(b)). FDG  $K_1$  was further compared to the Rb reference MBF for analyzing the relation between them using the generalized Renkin-Crone model (Fig.3). The resulting EFC was then used to convert FDG  $K_1$  to MBF. The results showed that the FDG-derived MBF correlated well with Rb MBF and glucose normalization for FDG  $K_1$  was important (Fig.4, Table 5). The extraction fraction of FDG demonstrated to be close to that of Rb-chloride (Fig. 5). Hence, FDG  $K_1$  quantification with the glucose-normalized EFC has the potential to provide MBF. Further studies on larger cohorts are warranted by these initial results.

The patient study is complex to do as it consists of both a dynamic FDG-PET scan and a dynamic Rb-PET scan, making patient accrual challenging. The sample size was small in this pilot study. The results mainly provided a report to warrant future studies. The analysis of this study was also limited to evaluation of global myocardial quantification instead of segment-level investigation to reduce the effect of noise. The noise performance of the scanner (2002 GE Discovery ST model) used in this study was far from optimal for exploring segment-based  $K_1$ , as indicated by the result from the previous identifiability analysis [31].

While motion correction was not included in the study, the effect of motion was less likely to result in a significant change to the results that were based on a large ROI given the spatial resolution of the PET scanner is only about 6-8 mm. A global ROI, however, may involve the spill-over effect from the right ventricle. The kinetic model used for FDG and Rb data in this study does not explicitly include the blood fraction from the right ventricle

but only the left ventricle. This is reasonable given the temporal sampling for the early phase of the dynamic scan was relatively coarse (10 s/frame). The TACs extracted from the left ventricle and right ventricle could be very close to each other. The separate estimation of  $v_{LV}$  and  $v_{RV}$  parameters in [31] is therefore implicitly combined into a single blood volume parameter  $v_b$  in Eq. (3). This is not uncommon. For example, Lortie *et al* also used a temporal sampling of 10 s/frame and single blood volume parameter for both  $^{13}\text{N}$ -ammonia and  $^{82}\text{Rb}$  studies.

Increase of temporal sampling, for example to 5 s/frame or 2 s/frame, has the potential to improve the separation of blood fractions from the left ventricle and right ventricle, and may lead to more robust estimation of FDG  $K_1$ . In particular, latest clinical PET scanners have an effective sensitivity gain of 4-25 fold and higher spatial resolution as compared to a typical conventional scanner GE Discovery 690 (see Table IV in [34]), and are remarkably better than the GE DST scanner used in this study. The EXPLORER total-body PET/CT scanner [35,36] has an ultrahigh sensitivity for dynamic imaging, making it more feasible to explore higher temporal resolution and even pixel-wise parametric imaging in the myocardium. Furthermore, improved dynamic image reconstruction using machine learning concepts has been developed for dynamic PET imaging, e.g. with the kernel methods (e.g. [37,38]) or deep neural-network methods (e.g. [39,40]) as recent examples. Thus, the progress in PET instrumentation and algorithms may provide a future opportunity to exploit higher temporal resolution, higher spatial resolution, and also motion-corrected segment-based quantification for a better study design for enhanced evaluations of myocardial blood flow using these FDG methods.

## 5. Conclusion

This pilot study demonstrates that FDG delivery rate  $K_1$  from a one-hour dynamic scan was closely associated with MBF in the myocardium, especially after an adjustment for blood glucose levels. With the glucose normalization and extraction fraction correction that convert FDG  $K_1$  to MBF, the FDG-derived MBF highly correlated with Rb MBF. The results also suggest FDG may have a first-pass myocardial extraction fraction similar to that of Rb-chloride. This work warrants a future, large study to further explore the potential of FDG for simultaneous imaging of myocardial blood flow and glucose metabolism.

## Acknowledgments

The authors thank the anonymous reviewers for their very helpful review comments. This work was supported in part by National Institutes of Health (NIH) under grant no. R21 HL131385 and American Heart Association under grant no. 15BGIA25780046. The work of J.E.L. is also supported in part by the Harold S. Geneen Charitable Trust Awards Program and the National Center for Advancing Translational Sciences, NIH, grant number UL1 TR001860 and linked award KL2 TR001859. The authors thank Denise Caudle, Michael Rusnak, and Ben Spencer for their assistance in the dynamic PET/CT data acquisition, Diana Ramos for her efforts in patient recruitments, and the patients that agreed to participate in

these studies.

## 6. Appendix

The relation between FDG  $K_1$  and blood flow  $F$  can be described by the Renkin-Crone (RC) model without a specific consideration of capillary recruitment [23],

$$K_1 = F \cdot \left[ 1 - \exp\left(-\frac{PS}{F}\right) \right] \triangleq RC(F; PS), \quad (13)$$

where  $P$  denotes the permeability of FDG and  $S$  is the surface area of a given section of the capillary bed. Here, the RC model is also denoted as a function of  $F$  and  $PS$  for convenient use. Following the classic Michaelis-Menten model, the product  $PS$  relates to the blood glucose concentration  $C_{\text{glu}}$  following the form [23, 41, 42],

$$PS = \frac{V_{m,\text{FDG}}}{K_{m,\text{FDG}} + \frac{K_{m,\text{FDG}}}{K_{m,\text{glu}}} C_{\text{glu}}} \triangleq MM(C_{\text{glu}}), \quad (14)$$

where  $V_{m,\cdot}$  is the maximal rate of FDG (or glucose) transfer and  $K_m$  denotes the concentration of FDG (or glucose) at which the half-maximum transfer rate is reached.

Based on the above two models, FDG  $K_1$  can be further expressed as a direct function of  $C_{\text{glu}}$ , i.e.,

$$K_1 \triangleq f(C_{\text{glu}}) = RC\left(F; MM(C_{\text{glu}})\right). \quad (15)$$

By expanding  $K_1$  at a reference blood glucose level  $C_{\text{glu},0}$  using the first-order Taylor's expansion, we will have the following linear approximation,

$$K_1 \approx f(C_{\text{glu},0}) + \dot{f}(C_{\text{glu},0}) \cdot (C_{\text{glu}} - C_{\text{glu},0}), \quad (16)$$

where  $\dot{f}(C_{\text{glu},0})$  is the first-order derivative of  $f$  at  $C_{\text{glu},0}$ ,

$$\dot{f}(C_{\text{glu},0}) = \left( \frac{\partial K_1}{\partial PS} \cdot \frac{\partial PS}{\partial C_{\text{glu}}} \right)_{C_{\text{glu}}=C_{\text{glu},0}}. \quad (17)$$

From Eq. (13), we have

$$\frac{\partial K_1}{\partial PS} = \frac{\partial RC(F; PS)}{\partial PS} = \exp\left(-\frac{PS}{F}\right) > 0, \quad (18)$$

and from Eq. (14), we have

$$\frac{\partial PS}{\partial C_{\text{glu}}} = \frac{\partial MM(C_{\text{glu}})}{\partial C_{\text{glu}}} = -\frac{V_{m,\text{FDG}} \frac{K_{m,\text{FDG}}}{K_{m,\text{glu}}}}{\left(K_{m,\text{FDG}} + \frac{K_{m,\text{FDG}}}{K_{m,\text{glu}}} C_{\text{glu}}\right)^2} < 0. \quad (19)$$

Combing the above two relations together produces

$$\dot{f}(C_{\text{glu},0}) < 0. \quad (20)$$

Thus, the approximate linear relation of FDG  $K_1$  with the blood glucose level  $C_{\text{glu}}$  can be re-expressed as

$$K_1 \approx -s \cdot C_{\text{glu}} + int, \quad (21)$$

where the absolute slope  $s$  and the intercept  $int$  relate to the reference blood glucose level  $C_{glu,0}$  via

$$s = -\dot{f}(C_{glu,0}) > 0, \quad int = f(C_{glu,0}) + s \cdot C_{glu,0}. \quad (22)$$

## References

- [1] T. H. Schindler, H. R. Schelbert, A. Quercioli, V. Dilsizian, "Cardiac PET Imaging for the Detection and Monitoring of Coronary Artery Disease and Microvascular Health," *JACC: Cardiovascular Imaging*, 3(6): 623-640, 2010.
- [2] P. A. Kaufmann, P. G. Camici, "Myocardial Blood Flow Measurement by PET: Technical Aspects and Clinical Applications," *Journal of Nuclear Medicine*, 46(1): 75-88, 2005.
- [3] MF Di Carli, S Dorbala, J Meserve, *et al.*, "Clinical myocardial perfusion PET/CT," *Journal of Nuclear Medicine*, 48(5): 783-793, 2007.
- [4] VL Murthy, TM Bateman, RS Beanlands, *et al.*, "Clinical Quantification of Myocardial Blood Flow Using PET: Joint Position Paper of the SNMMI Cardiovascular Council and the ASNC," *Journal of Nuclear Medicine*, 59(2):273-293, 2018.
- [5] J. Maddahi, R. R. S. Packard, "Cardiac PET Perfusion Tracers: Current Status and Future Directions," *Seminar in Nuclear Medicine*, 44(5): 333-43, 2014.
- [6] H Iida, I Kanno, A Takahashi, *et al.*, "Measurement of absolute myocardial blood flow with  $H_2^{15}O$  and dynamic positron-emission tomography. Strategy for quantification in relation to the partial-volume effect," *Circulation*, 78(1): 104-115, 1988.
- [7] I Danad, V Uusitalo, T Kero, *et al.*, "Quantitative Assessment of Myocardial Perfusion in the Detection of Significant Coronary Artery Disease Cutoff Values and Diagnostic Accuracy of Quantitative [ $^{15}O$ ]H $_2$ O PET Imaging," *Journal of the American College of Cardiology*, 64(14): 1464-1475, 2014
- [8] O. Muzik, RS Beanlands, GD Hutchins, *et al.*, "Validation of nitrogen-13-ammonia tracer kinetic model for quantification of myocardial blood flow using PET," *Journal of Nuclear Medicine*, 34(1): 83-91, 1993.
- [9] P J Slomka, E Alexanderson, R Jácome, *et al.*, "Comparison of Clinical Tools for Measurements of Regional Stress and Rest Myocardial Blood Flow Assessed with  $^{13}N$ -Ammonia PET/CT," *Journal of Nuclear Medicine*, 53(2): 171-181, 2012.
- [10] NA Mullani, RA Goldstein, KL Gould, *et al.*, "Myocardial perfusion with rubidium-82. I. Measurement of extraction fraction and flow with external detectors," *Journal of Nuclear Medicine*, 24(10): 898-906, 1983.
- [11] M Lortie, RSB Beanlands, K Yoshinaga, *et al.*, "Quantification of myocardial blood flow with  $^{82}Rb$  dynamic PET imaging," *European journal of nuclear medicine and molecular imaging*, 34(11): 1765-1774, 2007.
- [12] K. Yoshida, N. Mullani, K. L. Gould, "Coronary flow and flow reserve by PET simplified for clinical applications using rubidium-82 or nitrogen-13-ammonia," *Journal of Nuclear Medicine*, 37(10):1701-1712., 1996.
- [13] G El Fakhri, A Kardan, A Sitek, *et al.*, "Reproducibility and Accuracy of Quantitative Myocardial Blood Flow Assessment with  $^{82}Rb$  PET: Comparison with  $^{13}N$ -Ammonia PET," *Journal of Nuclear Medicine*, 50(7): 1062-1071, 2009.
- [14] SV Nesterov, E Deshayes, R Sciagrà, *et al.*, "Quantification of Myocardial Blood Flow in Absolute Terms Using  $^{82}Rb$  PET Imaging: The RUBY-10 Study," *JACC: Cardiovascular Imaging*, 7(11): 1119-1127, 2014.
- [15] J. Maddahi, "Properties of an ideal PET perfusion tracer: new PET tracer cases and data," *Journal of Nuclear Cardiology*, 19(suppl 1): S30-37, 2012.
- [16] van den Hoff J, Burchert W, Borner AR, *et al.*, " $^{11}C$ -11 Acetate as a quantitative perfusion tracer in myocardial PET," *Journal of Nuclear Medicine*, 42(8):1174-82, 2001.
- [17] Sciacca RR, Akinboboye O, Chou RL, Epstein S, Bergmann SR. "Measurement of myocardial blood flow with PET using  $^{11}C$ -11-acetate.," *Journal of Nuclear Medicine*, 42(1):63-70, 2001.

- [18] Timmer SAJ, Lubberink M, Germans T, *et al.*, “Potential of C-11 acetate for measuring myocardial blood flow: Studies in normal subjects and patients with hypertrophic cardiomyopathy,” *Journal of Nuclear Cardiology*, 17(2):264-75, 2010.
- [19] A Abraham, G Nichol, KA Williams, *et al.*, “F-18-FDG PET Imaging of Myocardial Viability in an Experienced Center with Access to F-18-FDG and Integration with Clinical Management Teams: The Ottawa-FIVE Substudy of the PARR 2 Trial,” *Journal of Nuclear Medicine*, 51(4): 567-574, 2010.
- [20] P. G. Camici, S. K. Prasad, and O. E. Rimoldi, “Stunning, hibernation, and assessment of myocardial viability,” *Circulation*, 117(1): 103-114, 2008.
- [21] H. Yamagishi, N. Shirai, M. Takagi, M. Yoshiyama, K. Akioka, K. Takeuchi, J. Yoshikawa. “Identification of Cardiac Sarcoidosis with <sup>13</sup>N-NH<sub>3</sub>/<sup>18</sup>F-FDG PET,” *Journal of Nuclear Medicine*, 44 (7) 1030-1036, 2003.
- [22] J. Maddahi, J. Lazewatsky, J. E. Udelson, *et al.*, “Phase-III Clinical Trial of Fluorine-18 Flurpiridaz Positron Emission Tomography for Evaluation of Coronary Artery Disease,” *Journal of the American College of Cardiology*, 76(4): 391-401, 2020.
- [23] R. E. Carson, “Tracer Kinetic Modeling in PET,” in *Positron Emission Tomography*, D. L. Bailey, D. W. Townsend, P. E. Valk, and M. N. Maisey Eds. Springer London, pp 127-159, 2005.
- [24] J Tseng, LK Dunnwald, EK Schubert, *et al.*, “Correlation with tumor blood flow and changes in response to neoadjuvant chemotherapy,” *Journal of Nuclear Medicine*, 45(11): 1829-1837, 2004.
- [25] N. A. Mullani, R. S. Herbst, R. G. O’Neil, *et al.*, “Tumor blood flow measured by PET dynamic imaging of first-pass F-18-FDG uptake: A comparison with O-15-Labeled water-measured blood flow,” *Journal of Nuclear Medicine*, 49(4): 517-523, 2008.
- [26] H. Bernstine, M Braun, N Yefremov, *et al.*, “FDG PET/CT Early Dynamic Blood Flow and Late Standardized Uptake Value Determination in Hepatocellular Carcinoma,” *Radiology*, 260(2): 503-510, 2011.
- [27] A Cochet, S Pigeonnat, B Khoury, *et al.*, “Evaluation of Breast Tumor Blood Flow with Dynamic First-Pass F-18-FDG PET/CT: Comparison with Angiogenesis Markers and Prognostic Factors,” *Journal of Nuclear Medicine*, 53(4): 512-520, 2012.
- [28] O Humbert, M Lasserre, A Bertaut, *et al.*, “Breast Cancer Blood Flow and Metabolism on Dual-Acquisition F-18-FDG PET: Correlation with Tumor Phenotype and Neoadjuvant Chemotherapy Response,” *Journal of Nuclear Medicine*, 59(7): 1035-1041, 2018.
- [29] M. Winterdahl, O. L. Munk, M. Sorensen, F. V. Mortensen, and S. Keiding. “Hepatic Blood Perfusion Measured by 3-Minute Dynamic F-18-FDG PET in Pigs,” *Journal of Nuclear Medicine*, 52(7): 1119-1124, 2011.
- [30] M. Walberer, H Backes, MA Rueger, *et al.*, “Potential of Early F-18 -2-Fluoro-2-Deoxy-D-Glucose Positron Emission Tomography for Identifying Hypoperfusion and Predicting Fate of Tissue in a Rat Embolic Stroke Model,” *Stroke*, 43(1): 193-198, 2012.
- [31] Y. Zuo, RD Badawi, C. Foster, T. Smith, J. Lopez, and G. Wang, “Multiparametric cardiac <sup>18</sup>F-FDG PET in humans: kinetic model selection and identifiability analysis,” *IEEE Transactions on Radiation in Plasma and Medical Sciences*, 4(6): 759-767, 2020.
- [32] M. D. Cerqueira, N. J. Weissman, V. Dilsizian, *et al.*, “Standardized myocardial segmentation and nomenclature for tomographic imaging of the heart - A statement for healthcare professionals from the Cardiac Imaging Committee of the Council on Clinical Cardiology of the American Heart Association,” *Circulation*, vol. 105, no. 4, pp. 539-542, Jan 2002,
- [33] D. B. Stout, S. C. Huang, W. P. Melega, M. J. Raleigh, M. E Phelps, J. R. Barrio, “Effects of large neutral amino acid concentrations on 6-[F-18]Fluoro-L-DOPA kinetics,” *J Cereb Blood Flow Metab*, 18(1):43-51, 1998.
- [34] G. Wang, A. Rahmim, R. N. Gunn, “PET parametric imaging: past, present, and future,” *IEEE Transactions on Radiation and Plasma Medical Sciences*, 4(6): 663 - 675, 2020.
- [35] S. Cherry, R. Badawi, J. Karp, W. Moses, P. Price, and T. Jones, “Total-body imaging: Transforming the role of PET in translational medicine,” *Science Translational Medicine*, vol. 9, no. 381, p. eaaf6169, 2017.

- [36] R. Badawi, H Shi, P Hu, *et al.*, “First human imaging studies with the EXPLORER total-body PET scanner,” *Journal of Nuclear Medicine*, vol. 60, no. 3, pp. 299-303, 2019.
- [37] G. Wang, J. Qi, “PET image reconstruction using kernel method,” *IEEE Transactions on Medical Imaging*, vol. 34, no. 1, pp. 61-71, 2015.
- [38] G. Wang, “High temporal-resolution dynamic PET image reconstruction using a new spatiotemporal kernel method,” *IEEE Transactions on Medical Imaging*, vol. 38, no. 3, pp. 664 – 674, 2019.
- [39] A. Reader, G. Corda, A. Mehranian, C. da Costa-Luis, S. Ellis, and J. Schnabel, “Deep Learning for PET Image Reconstruction,” *IEEE Transactions on Radiation and Plasma Medical Sciences*, 5(1): 1-25, 2020.
- [40] K. Gong, J. Guan, K. Kim, *et. al.*, “Iterative PET Image Reconstruction Using Convolutional Neural Network Representation,” *IEEE Transactions on Medical Imaging*, vol. 38, no. 3, pp. 675-685, 2019.
- [41] A. Gjedde, “Rapid steady-state analysis of blood-brain glucose transfer in rat,” *Acta Physiol Scand*, 108(4):331-339, 1980.
- [42] A. Gjedde, “High- and low-affinity transport of D-glucose from blood to brain,” *Journal of Neurochemistry*, 36(4):1463-71, 1981.